Editors' Suggestion

Competing role of the *p* and *d* orbitals in the orbital angular momentum induced spin splitting of surface states on Au(110)

H. Ishida

College of Humanities and Sciences, Nihon University, Tokyo 156-8550, Japan

(Received 25 May 2023; accepted 21 July 2023; published 2 August 2023)

We investigate correlations between the spin-splitting energy and the orbital angular momentum (OAM) of the L-gap surface states on Au(110)-(1×1) and $-(1 \times 2)$ surfaces by first-principles calculations. It is revealed that their spin-splitting energies can be expressed approximately as $\Delta\varepsilon \approx 2|\xi_p \mathbf{L}^{(p)} + \xi_d \mathbf{L}^{(d)}|$, where $\mathbf{L}^{(p)}$ and $\mathbf{L}^{(d)}$ are the p- and d-orbital contributions to the OAM in the absence of spin-orbit interaction (SOI), and ξ_p and ξ_d are the atomic SOI parameters for the p and d orbitals of Au. For all the surface states studied, the major component $\mathbf{L}^{(d)}$ exhibits rather weak anisotropy in the space of two-dimensional wave vector $\mathbf{k}$, whereas the minor component $\mathbf{L}^{(p)}$ is more anisotropic between the $[\bar{1}10]$ and [001] directions. Since ξ_p for Au is several times larger than ξ_d, $\Delta\varepsilon$ becomes more strongly anisotropic than the total OAM $\mathbf{L}$ in the $\mathbf{k}$ space. In particular, the Rashba parameter in the [001] direction of the unoccupied surface band on the (1×1) surface becomes nearly vanishing due to strong cancellation of the p- and d-orbital contributions. We also discuss how the OAM of surface states calculated without SOI is modified when SOI is turned on.

DOI: 10.1103/PhysRevB.108.085401

I. INTRODUCTION

Currently, there is a large interest in the orbital Rashba effect at solid surfaces because of its potential technological applications. Its key quantity is the orbital angular momentum (OAM) induced in the wave function of surface states due to inversion symmetry breaking (ISB) [1–10]. The OAM of a surface band is locked to two-dimensional wave vector $\mathbf{k}$ and exhibits a chiral texture around a symmetry point in the surface Brillouin zone (SBZ), which is similar to the chiral texture of electron spin resulting from spin-orbit interaction (SOI) due to surface potential gradient [11]. However, the orbital Rashba effect is independent of SOI and occurs by the ISB at the surface alone. To describe the subsequent spin splitting of a surface state, one does not need the aforementioned surface-specific SOI. Instead, one only needs the standard atomic SOI of the form $\hat{H}_{\rm so} = \lambda\, \vec{L} \cdot \vec{\sigma}$, where $\vec{L}$ and $\vec{\sigma}$ are the local OAM operator and a vector of the Pauli matrices, respectively. In the strong SOI regime, the OAM and electron spin are strongly coupled mutually so their relative directions in the resulting two spin-split states are the same. On the other hand, in the weak SOI regime, the OAM acts as an effective magnetic field to spin polarize the surface state so the electron spin is oriented parallel to the OAM in the higher spin-split state and is antiparallel to the OAM in the lower spin-split state.

Kim *et al.* [3] revealed that the spin splitting of the L-gap surface state on Au(111) [12,13] and Cu(111) [14] originates from the orbital Rashba effect in the weak SOI regime. The OAM of the two spin-split surface bands exhibits a clockwise chiral texture around $\bar{\Gamma}$ ($\mathbf{k} = 0$) seen from the vacuum, whereas the electron spin of the upper and lower spin-split bands exhibits clockwise and counterclockwise chiral textures, respectively. More interestingly, while the wave function of the L-gap surface state has strong p_z character (the z axis is the surface normal), the momentum-locked OAM originates dominantly from the d orbitals with much smaller weight than p_z [15,16].

Surface states associated with the L point bulk band gap also emerge on (110) surfaces of Cu, Ag, and Au [17–25]. For the (1×1) surfaces of Cu and Ag, they appear near the $\bar{Y}$ point in the SBZ, onto which the bulk L point is projected. On the unreconstructed Au(110) surface, a partially occupied surface band with anisotropic energy dispersion similar to the one on Cu(110) [25] was observed by angle-resolved photoemission spectroscopy (ARPES) [24]. In contrast, on the missing-row reconstructed Au(110) surface, inverse photoemission experiments and density functional theory (DFT) calculations have revealed that this band is shifted upward and becomes unoccupied [18–20,24]. For both (1×1) and (1×2) surfaces, Nagano *et al.* [26] calculated anisotropic spin-splitting energies of the lowest surface band. Simon *et al.* analyzed the spin splitting of the partially occupied surface band on the (1×1) surface using the $\mathbf{k} \cdot \mathbf{p}$ perturbation theory. Yet, it was only very recently that the spin splitting of the L-gap surface states on Au(110) was observed experimentally [27].

In the present paper, we study the OAM-induced spin splitting of the L-gap surface states on semi-infinite Au(110) surfaces by first-principles DFT calculations. We will demonstrate that the calculated spin-splitting energy $\Delta\varepsilon$ can be explained by the expression derived from perturbation theory, $\Delta\varepsilon \approx 2|\xi_p \mathbf{L}^{(p)} + \xi_d \mathbf{L}^{(d)}|$, where $\mathbf{L}^{(p)}$ and $\mathbf{L}^{(d)}$ are the p- and d-orbital contributions to the OAM of the surface states calculated in the absence of SOI, and ξ_p and ξ_d are the atomic SOI parameters of Au. We show that while $\mathbf{L}^{(d)}$ is much larger than $\mathbf{L}^{(p)}$ as in the case of the corresponding ones on Au(111), the spin-splitting energy becomes more anisotropic than OAM,

since the weight of the more anisotropic $\mathbf{L}^{(p)}$ is amplified as ξ_p is several times larger than ξ_d. The cancellation of the p and d components leads to a very small Rashba parameter for the unoccupied surface band on Au(110)-(1 × 1) in the [001] direction.

The outline of this paper is as follows. In Sec. II, we briefly describe the method of the calculations. In Sec. III, we present results of DFT calculations for the unreconstructed and missing-row reconstructed Au(110) surfaces and elucidate the interconnection between the spin splitting and the OAM of the L-gap surface states. In addition, we present a general discussion on how the OAM of a surface state is modified when SOI is turned on. We conclude in Sec. IV.

II. METHOD OF CALCULATION

The atomic structure of the unreconstructed and missing-row reconstructed Au(110) surfaces is determined by total-energy minimization within generalized gradient approximation (GGA) in DFT, where we adopt the Perdew-Burke-Ernzerhof (PBE) exchange-correlation energy functional [28]. Calculations are made by using the VIENNA AB INITIO SIMULATION PACKAGE (VASP) [29,30], an implementation of the projector augmented-wave method [31]. For both systems, the surface is represented by a 13-layer periodic slab model, where the outer five atomic layers on both sides are relaxed and the three central layers are fixed at bulk positions. The bulk lattice constant of Au, which determines atomic positions of the central layers, is chosen as $a_{\rm cal} = 4.16$ Å derived from a separate bulk calculation for Au in face-centered-cubic (FCC) structure.

The electronic structure of semi-infinite Au(110) surfaces is calculated by an embedded Green's-function (EGF) program [16] that combines the embedding theory of Inglesfield [32,33] and the full-potential linearized augmented plane-wave (LAPW) approach [34]. The SOI inside the muffin-tin (MT) sphere surrounding each atomic core is incorporated by the standard $\vec{L}\cdot\vec{\sigma}$ term. We note that while full-relativistic approaches based on the Dirac equation [35–38] might be necessary for heavier chemical elements such as actinides, the present formalism combining the scalar-relativistic Hamiltonian with the atomic SO term is accurate enough for Au. For example, the energy dispersion of the L-gap surface state on Au(111) calculated with the present formalism agrees well with that obtained by a full-relativistic calculation [35]. The plane-wave cutoff energy of the LAPW basis is chosen as $E_c = 3.5^2$ Ry and radial orbitals with angular momentum $l \leqslant 6$ are included in the basis functions within MT spheres of Au atoms. To be consistent with the structural calculation, we employ the GGA-PBE functional in performing the EGF calculations. We include eight to ten outermost atomic layers and the vacuum region in the embedded surface region for both the (1 × 1) and (1 × 2) surfaces.

Recently, we revealed that the binding energy of the L-gap surface state on Au(111) relative to the Fermi energy (E_F) is considerably underestimated as compared with the experimental one if the bulk lattice constant of Au is set to the GGA value instead of the experimental one, $a_{\rm exp} = 4.08$ Å [39]. To avoid similar underestimations, we multiplied surface atomic coordinates output by the VASP program by a factor of $f = a_{\rm exp}/a_{\rm cal} = 4.08/4.16 = 0.98$ and used these slightly modified atomic coordinates as the input to the EGF calculations. In the following, we use symbol a to mean $a_{\rm exp}$.

The output of the EGF calculation is the Green's function $\hat{G}(\mathbf{k}, \omega, \mathbf{r}, \mathbf{r}')$, where $\hat{G}$ is a 2 × 2 matrix with respect to spin index, $\omega = \varepsilon + i\gamma$ is a complex energy with $\gamma \geqslant 0$, and $\mathbf{r}$ and $\mathbf{r}'$ are position vectors in the embedded surface region. The $\mathbf{k}$-resolved DOS projected on the MT sphere of an atom located at $\mathbf{r}_a$ is defined by

$$\rho(\mathbf{k}, \varepsilon) = \frac{-1}{\pi}\int_{|\mathbf{r}-\mathbf{r}_a|\leqslant R} d\mathbf{r}\ \mathrm{Tr}[\mathrm{Im}\hat{G}(\mathbf{k}, \omega, \mathbf{r}, \mathbf{r})], \qquad (1)$$

where R is the MT sphere radius and trace is taken with respect to spin index.

III. RESULTS AND DISCUSSION

A. Au(110)-(1 × 1) surface

First, we present results for the unreconstructed (1 × 1) surface. The z axis is chosen as the surface normal pointing toward the vacuum ([110] direction), and the x and y axes are chosen as the $[\bar{1}10]$ and [001] directions, respectively. The origin of the (x, y, z) coordinates is placed at one of the first-layer atoms. The surface has mirror reflection symmetry about four vertical cut-planes, $x = 0$ (the yz plane), $x = \frac{a}{2\sqrt{2}}$, $y = 0$ (the xz plane), and $y = \frac{a}{2}$. The corresponding operators will be denoted by $\hat{M}_x(0)$, $\hat{M}_x(\frac{a}{2\sqrt{2}})$, $\hat{M}_y(0)$, and $\hat{M}_y(\frac{a}{2})$.

In Fig. 1(a), we show a logarithmic intensity plot of $\rho(\mathbf{k}, \varepsilon)$ for a first-layer surface atom along the $\bar{Y}\bar{\Gamma}$ and $\bar{Y}\bar{S}$ lines around the $\bar{Y}$ point with $\mathbf{k}_{\bar{Y}} = (0, \frac{\pi}{a})$ in the SBZ depicted in Fig. 1(b). In contrast to Au(111), which exhibits only one surface band within the surface-projected L-point bulk band gap [12], two parabolic-shaped, spin-split surface bands called S_1 and S_2 henceforth appear within the band gap. We denote the upper and lower branches of S_i by $S_i^{(+)}$ and $S_i^{(-)}$ and their energies at $\mathbf{k}$ by $\varepsilon_i^{(\pm)}(\mathbf{k})$ ($i = 1, 2$). The upper branches of S_1 and S_2 are spin-polarized clockwise around $\bar{Y}$, while their lower branches are spin polarized counterclockwise as seen from the vacuum. The spin-split dispersion curves of S_1 in Fig. 1(a) agree well with previous theoretical ones [24,26,40]. Experimentally, the anisotropic energy dispersion of S_1 on Au(110)-(1 × 1) was studied by ARPES, although its spin splitting was not observed [24]. To our knowledge, the unoccupied S_2 band on Au(110)-(1 × 1) has rarely been studied. This is in contrast to Cu(110) and Ag(110), for which the parabolic dispersion curve of S_2 with its bottom located at $1.5 - 2.0$ eV above E_F was observed by inverse photoemission spectroscopy [17,23]. On the theory side, the S_2 band with a parabolic dispersion curve similar to ours was reported in Fig. 4 of Ref. [24] without being mentioned.

Why two surface bands emerge in the case of the (110) surface is explained by the fact that two nonequivalent points in the bulk Brillouin zone, $L : \frac{\pi}{a}(\mathbf{e}_1 + \mathbf{e}_2 + \mathbf{e}_3)$ and $L' : \frac{\pi}{a}(-\mathbf{e}_1 - \mathbf{e}_2 + \mathbf{e}_3)$, are projected onto $\bar{Y}$, where $\mathbf{e}_1$, $\mathbf{e}_2$, and $\mathbf{e}_3$ are the unit vectors in the [100], [010], and [001] directions, respectively. As a consequence, when one plots the bulk complex band structure at $\bar{Y}$ as a function of k_z, the wave number in the normal direction, the real bands (Bloch states) exhibit a minimum and a maximum at both L ($k_z = \frac{\sqrt{2}\pi}{a}$) and L' ($k_z = -\frac{\sqrt{2}\pi}{a}$).

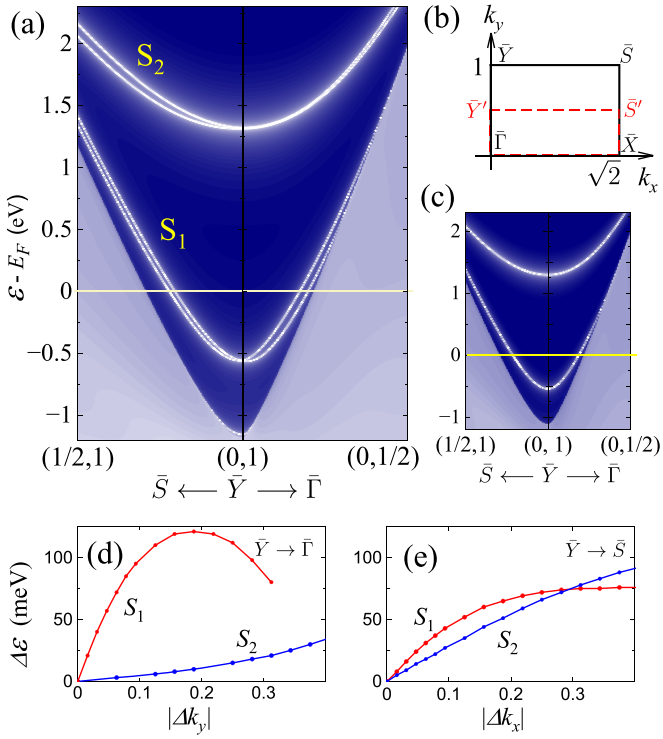

FIG. 1. (a) Logarithmic intensity plot of $\rho(\mathbf{k}, \varepsilon)$ for a first-layer atom on Au(110)-(1 × 1). Imaginary energy $\gamma = 0.5$ meV. (b) Surface Brillouin zone (SBZ) of Au(110)-(1 × 1) (solid line) and $-(1 \times 2)$ (red dashed line) surfaces. (c) The same as panel (a) except that SOI is turned off. (d), (e) Spin-splitting energies of the S_1 and S_2 surface bands along the $\bar{Y}\bar{\Gamma}$ and $\bar{Y}\bar{S}$ lines as a function of $\Delta\mathbf{k} = \mathbf{k} - \mathbf{k}_{\bar{Y}}$ with $\mathbf{k}_{\bar{Y}} = (0, \frac{\pi}{a})$. In all panels, wave vectors and wave numbers are in units of $\frac{\pi}{a}$ with a, the lattice constant of FCC Au.

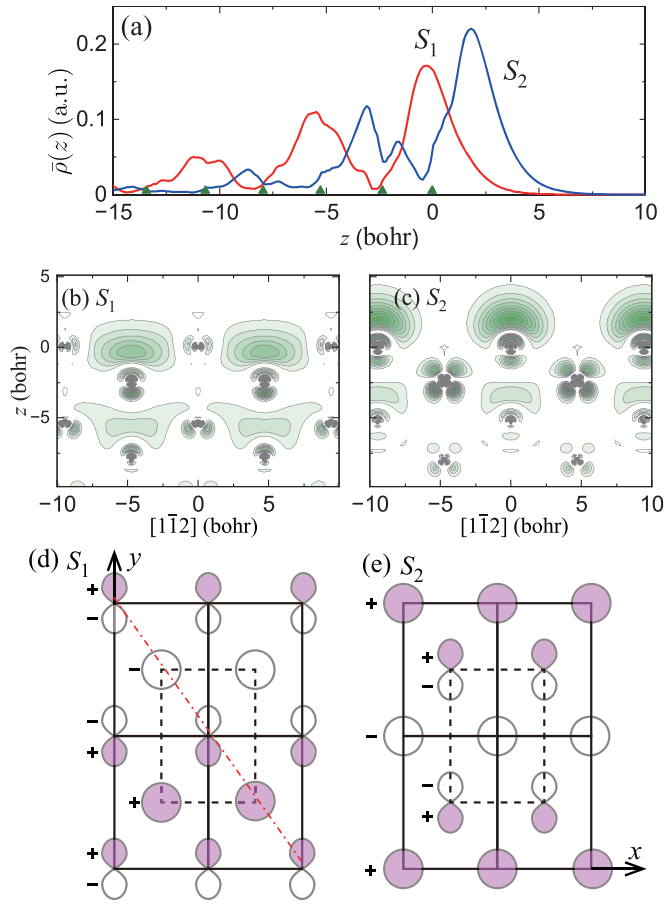

FIG. 2. (a) Planar-averaged charge densities of the doubly degenerate S_1 and S_2 states at $\bar{Y}$ on Au(110)-(1 × 1) in the presence of SOI. Solid triangles on the z axis show positions of the (110) lattice planes. (b), (c) Contour maps of the same charge densities as in (a) on a $(\bar{1}11)$ vertical cut-plane. (d), (e) Orbital composition of the wave function of S_1 and S_2 at $\bar{Y}$ in the absence of SOI. Solid and dashed lines illustrate (1 × 1) unit cells of odd-numbered and even-numbered lattice planes, respectively. Red dash-dotted line in (d) indicates the vertical cut-plane on which charge densities in (b) and (c) are plotted.

As a result, at both points, there appears a complex band with nonvanishing Imk_z (evanescent wave) that connects the minimum and maximum of the real bands. Since the surface-state wave function on the bulk side is expressed as a linear combination of the evanescent waves arising from both L and L', it has more chance of being smoothly connected to the decaying solution on the vacuum side than that for Au(111), for which evanescent waves on the bulk side arise only from the complex band at L.

To examine how strongly SOI modifies the two surface bands, we made an EGF calculation in which we turned off the SOI term while adopting the same self-consistent DFT potential. The obtained $\rho(\mathbf{k}, \varepsilon)$ for a first-layer atom is shown in Fig. 1(c). The energy dispersion with $\mathbf{k}$ of S_1 and S_2 hardly changes except that both bands become spin degenerate, which implies that SOI is not essential for the occurrence of S_1 and S_2. Instead, its main effect is to cause the spin splitting of S_1 and S_2. We plot in Figs. 1(d) and 1(e) the spin-splitting energies of the two bands, $\Delta\varepsilon = \varepsilon_i^{(+)}(\mathbf{k}) - \varepsilon_i^{(-)}(\mathbf{k})$ $(i = 1, 2)$ as a function of $\Delta\mathbf{k} = \mathbf{k} - \mathbf{k}_{\bar{Y}}$ along two symmetry lines in the SBZ. The curve for S_1 along $\bar{Y}\bar{\Gamma}$ ends at $|\Delta k_y| \sim 0.31\frac{\pi}{a}$, since $S_1^{(-)}$ is merged into the projected bulk band and disappears. Surprisingly, $\Delta\varepsilon$ for S_2 along $\bar{Y}\bar{\Gamma}$ at small Δk_y is by more than one order of magnitude smaller than the corresponding one for S_1. To elucidate the physical mechanism that produces this large difference is one of the main themes of the present paper.

Before doing so, we want to discuss the real-space symmetry and orbital character of the two surface bands. In Fig. 2(a), we show planar-averaged charge densities of the doubly degenerate S_1 and S_2 at $\bar{Y}$ as a function of z in the presence of SOI. We observe that S_2 has more weight on the vacuum side of the topmost Au layer. Also, its wave function decays more rapidly toward the interior of the metal than that of S_1. In Figs. 2(b) and 2(c), we show contour maps of the charge densities of the same states as in Fig. 2(a) on a $(\bar{1}11)$ vertical cut-plane, which bisects rectangular unit cells of the (110) lattice plane diagonally. In the absence of SOI, the wave function of S_1 is spin diagonal and as illustrated in Fig. 2(d), its spatial part at $\bar{Y}$ is odd with respect to $\hat{M}_y(0)$ and even with respect to $\hat{M}_y(\frac{a}{2})$, $\hat{M}_x(0)$, and $\hat{M}_x(\frac{a}{2\sqrt{2}})$. Thus, the spatial part of the wave function is made out of p_y and d_{yz} orbitals in odd-numbered layers and of s, p_z, $d_{x^2-y^2}$, and $d_{3z^2-r^2}$ orbitals in even-numbered layers. Although atomic orbitals with

TABLE I. Eigenvalues of S_1 and S_2 with respect to mirror reflection operators in the absence of and in the presence of SOI along $\bar{Y}\bar{\Gamma}$ and $\bar{Y}\bar{S}$ for Au(110)-(1 × 1).

SOI		$\bar{Y}\bar{\Gamma}$ $\hat{M}_x(0)$	$\hat{M}_x(\frac{a}{2\sqrt{2}})$	$\bar{Y}\bar{S}$ $\hat{M}_y(0)$	$\hat{M}_y(\frac{a}{2})$
No	S_1	$+1$	$+1$	-1	$+1$
	S_2	$+1$	$+1$	$+1$	-1
Yes	$S_1^{(+)}$	$+i$	$+i$	$-i$	$+i$
	$S_1^{(-)}$	$-i$	$-i$	$+i$	$-i$
	$S_2^{(+)}$	$+i$	$+i$	$+i$	$-i$
	$S_2^{(-)}$	$-i$	$-i$	$-i$	$+i$

opposite spin directions and opposite spatial parities are slightly mixed when SOI is turned on, the orbital character of S_1 at $\bar{Y}$ shown in Fig. 2(b) is well represented by that in Fig. 2(d).

As seen from Fig. 2(e), the symmetry of the wave function of S_2 at $\bar{Y}$ is identical with that of S_1, if it is spatially translated by a lattice vector $\mathbf{d} = \frac{a}{2\sqrt{2}}(1, \sqrt{2}, -1)$ connecting two lattice points in neighboring (110) planes. This may also be seen in Figs. 2(b) and 2(c) where the charge density of S_2 in Fig. 2(c) looks similar to that of S_1 in Fig. 2(b) if the former is translated by $\mathbf{d}$ toward the interior of the metal. Why this can occur is again attributed to the complex band structure at $\bar{Y}$: One can construct two evanescent waves related by $\mathbf{d}$ from the two independent complex bands arising from L and L'. Therefore, the large difference in the spin-splitting energies between S_1 and S_2 in Fig. 1(d) cannot be ascribed to the different orbital symmetry of the two states [8]. Off the $\bar{Y}$ point, the wave functions of S_1 and S_2 are eigenfunctions of $\hat{M}_x(0)$ and $\hat{M}_x(\frac{a}{2\sqrt{2}})$ along $\bar{Y}\bar{\Gamma}$, and eigenfunctions of $\hat{M}_y(0)$ and $\hat{M}_y(\frac{a}{2})$ along $\bar{Y}\bar{S}$. We tabulate their eigenvalues in the absence and in the presence of SOI in Table I.

The energy dispersion curves of S_1 and S_2 along $\bar{Y}\bar{\Gamma}$ and $\bar{Y}\bar{S}$ can be approximated in the vicinity of $\bar{Y}$ as

$$\varepsilon_i^{(\pm)}(\mathbf{k}) = E_0 + \frac{\hbar^2}{2m^*}|\Delta\mathbf{k}|^2 \pm \alpha_R|\Delta\mathbf{k}|, \tag{2}$$

where m^* is the electron effective mass and α_R is the so-called Rashba parameter. We observe from Figs. 1(d) and 1(e) that the linear energy splitting as implied by Eq. (2), $\Delta\varepsilon = 2\alpha_R|\Delta\mathbf{k}|$, holds only for $|\Delta\mathbf{k}| \lesssim 0.1\frac{\pi}{a}$. The α_R parameters evaluated by least squares fitting with the calculated surface state energies in the interval $[0, k_m]$ with $k_m = 0.08\frac{\pi}{a} = 0.06\,\text{Å}^{-1}$ are listed in Table II. They are strongly anisotropic, and, as mentioned in the above, the one for S_2 along $\bar{Y}\bar{\Gamma}$ is surprisingly small. We also estimated m^* by fitting the calculated $\frac{1}{2}(\varepsilon_i^{(+)} + \varepsilon_i^{(-)})$ with the function $E_0 + \frac{\hbar^2}{2m^*}|\Delta\mathbf{k}|^2$. The m^* values without brackets in Table II were obtained by using a fitting interval $[0, k_m]$ with $k_m = 0.08\frac{\pi}{a}$, while we used a wider interval with $k_m = 0.32\frac{\pi}{a} = 0.24\,\text{Å}^{-1}$ for the second ones in brackets. That m^* of S_1 obtained by fitting increases significantly with increasing k_m implies that Eq. (2) holds only in a small range of $|\Delta\mathbf{k}|$. By ARPES, Nuber *et al.*[24] reported $m^* = (0.25 \pm 0.01)m_e$ for S_1 along $\bar{Y}\bar{S}$, which agrees well with the present value derived with $k_m = 0.32\frac{\pi}{a}$.

TABLE II. Parameters describing the spin-split energy dispersion curves of the L-gap surface states on Au(110) surfaces along the [001] and [$\bar{1}$10] directions. E_0 is measured relative to E_F. The first and second (in brackets) m^* values were estimated by using a fitting interval $[0, k_m]$ with $k_m = 0.08\frac{\pi}{a}$ and $k_m = 0.32\frac{\pi}{a}$, respectively. α_R was estimated by using $k_m = 0.08\frac{\pi}{a}$.

		E_0 (eV)	m^*/m	α_R (eVÅ)
(1 × 1) S_1	$\bar{Y}\bar{\Gamma}$	−0.56	0.11 (0.17)	0.74
	$\bar{Y}\bar{S}$	−0.56	0.14 (0.22)	0.32
(1 × 1) S_2	$\bar{Y}\bar{\Gamma}$	1.31	0.53 (0.49)	0.02
	$\bar{Y}\bar{S}$	1.31	0.62 (0.65)	0.19
(1 × 2) S_1	$\bar{\Gamma}\bar{Y}'$	0.12	0.29 (0.28)	0.64
	$\bar{\Gamma}\bar{X}$	0.12	0.22 (0.29)	0.32

Let us now demonstrate that the anisotropic spin splitting of the two surface bands originates from the orbital Rashba effect. The orbital Rashba effect occurs even without SOI. Moreover, comparison of Figs. 1(a) and 1(c) suggests that the spin splitting of the two surface bands via SOI can be treated by perturbation theory. Therefore, we first calculate the OAM of surface states in the absence of SOI. Within the atom-centered approximation, the OAM of a surface state with the spatial part of the wave function Φ is given by

$$\mathbf{L} = \langle\Phi|\vec{L}|\Phi\rangle = \langle\Phi|\sum_a \vec{L}_a|\Phi\rangle, \tag{3}$$

where $\vec{L}_a = (\mathbf{r} - \mathbf{r}_a) \times \hat{\mathbf{p}}$ with momentum operator $\hat{\mathbf{p}}$ is the local angular momentum operator of an atom placed at $\mathbf{r}_a$, the volume integration is performed inside the MT sphere surrounding the atomic core, and summation is taken over all atoms. Inside each MT sphere, Φ can be expanded as $\Phi = \sum_{l\geqslant 0}\Phi_l$, where $\Phi_l = \sum_{|m|\leqslant l} Y_{lm}\,\phi_{lm}(|\mathbf{r} - \mathbf{r}_a|)$ with spherical harmonics Y_{lm}. We denote the contributions of $\Phi_{l=1}$ and $\Phi_{l=2}$ to $\mathbf{L}$ by $\mathbf{L}^{(p)}$ and $\mathbf{L}^{(d)}$, respectively.

The vector plots in Figs. 3(a) and 3(b) illustrate the $\mathbf{k}$-space distribution of the planar components of $\mathbf{L}^{(p)}$ and $\mathbf{L}^{(d)}$ for the S_1 band in the vicinity of $\bar{Y}$. The corresponding ones for S_2 are shown in Figs. 4(a) and 4(b). We used different scales for the length of vectors representing $\mathbf{L}^{(p)}$ and $\mathbf{L}^{(d)}$ to better illustrate the smaller p component. The z component of $\mathbf{L}$ is negligibly small and is not shown. From Figs. 3 and 4, we see that the $\mathbf{L}^{(p)}$ is small but nonnegligible and oriented mostly opposite the major component $\mathbf{L}^{(d)}$. Also, $\mathbf{L}^{(p)}$ exhibits stronger anisotropy between $\bar{Y}\bar{\Gamma}$ and $\bar{Y}\bar{S}$ than $\mathbf{L}^{(d)}$. Looking into more details, we see that while $|(\mathbf{L}^{(p)})_x|$ for S_1 is very small, $|(\mathbf{L}^{(p)})_x|$ for S_2 amounts to more than 20% of $|(\mathbf{L}^{(d)})_x|$. As for the y component, $|(\mathbf{L}^{(p)})_y|$ increase linearly with Δk_x as does $|(\mathbf{L}^{(d)})_y|$, and its magnitude is as large as $7 - 10\%$ of $|(\mathbf{L}^{(d)})_y|$ for both bands. The $\mathbf{k}$-space distributions of the major component $\mathbf{L}^{(d)}$ for the two bands shown in Figs. 3(b) and 4(b) are qualitatively similar. They exhibit a clockwise chiral texture around $\bar{Y}$ and rather weak anisotropy between $\bar{Y}\bar{\Gamma}$ and $\bar{Y}\bar{S}$. We show in Figs. 3(c) and 4(c) the total OAM for the two surface bands. Since $|\mathbf{L}^{(d)}|$ is much larger than $|\mathbf{L}^{(p)}|$, $\mathbf{L}$ is not very distinguishable from $\mathbf{L}^{(d)}$ at first glance.

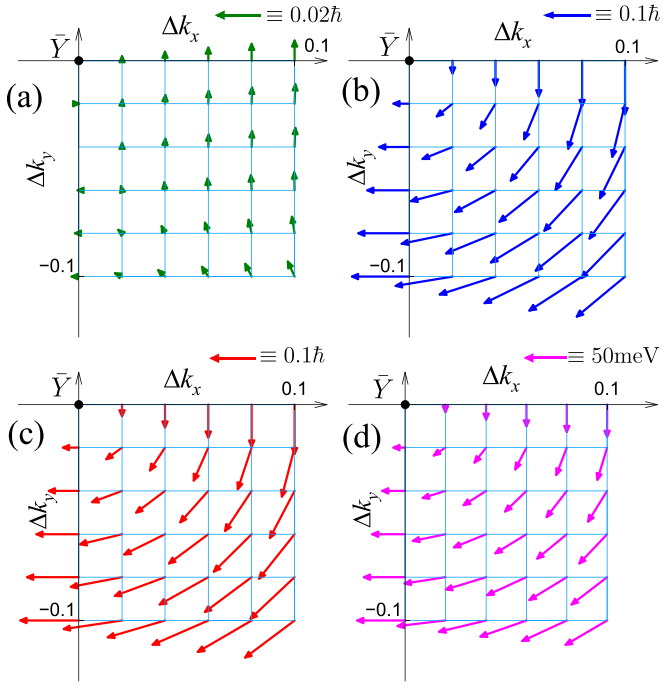

FIG. 3. The **k**-space distribution around $\bar{Y}$ of (a) $\mathbf{L}^{(p)}$, (b) $\mathbf{L}^{(d)}$, and (c) the total OAM **L** for the S_1 band on Au(110)-(1 × 1) in the absence of SOI. (d) Vector field **U** inducing the spin splitting of the S_1 band around $\bar{Y}$. In all panels, Δk_x and Δk_y are given in units of $\frac{\pi}{a}$.

Now, we introduce the SOI term in the Hamiltonian,

$$\hat{H}_{\rm so} = \sum_a f_a(r)(\vec{L}_a \cdot \vec{\sigma}), \tag{4}$$

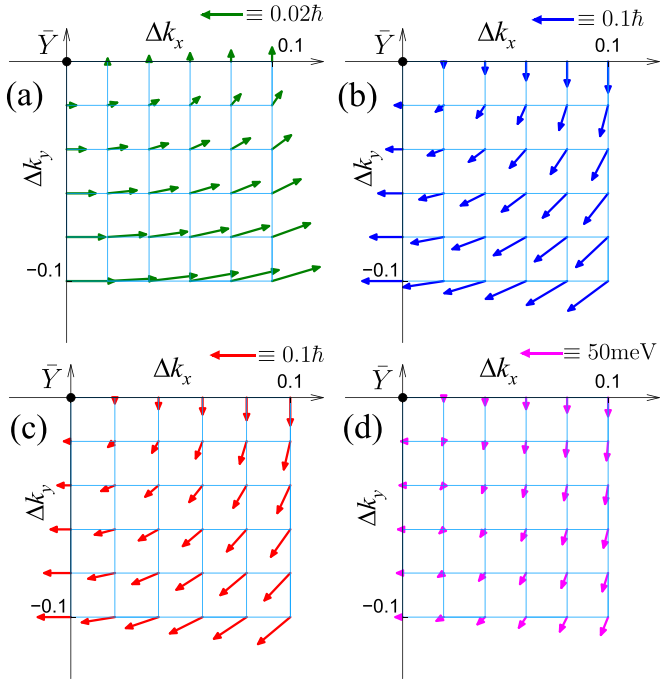

FIG. 4. The same as Fig. 3 for the S_2 band on Au(110)-(1 × 1).

with

$$f_a(r) = \frac{\hbar}{4M^2c^2}\frac{1}{r}\frac{dv_a(r)}{dr}, \quad M = m_e + \frac{\epsilon - v_a(r)}{2c^2}, \tag{5}$$

where $r = |\mathbf{r} - \mathbf{r}_a|$, c is light velocity and $v_a(r)$ is the spherical part of the one-electron DFT potential within the MT sphere centered at $\mathbf{r}_a$. According to the perturbation theory in the lowest-order of SOI, the spin Hamiltonian lifting the degeneracy of a surface state is given by $\Delta\hat{H} = \mathbf{U} \cdot \vec{\sigma}$ with

$$\mathbf{U} = \langle\Phi| \sum_a f_a(r)\vec{L}_a|\Phi\rangle, \tag{6}$$

where Φ is the spatial part of the wave function of the surface state in the absence of SOI. The energies of the resultant spin-split states are $\pm|\mathbf{U}|$ relative to the energy of the original spin degenerate state, and the upper and lower branches become spin polarized in the $\mathbf{e}_u$ and $-\mathbf{e}_u$ directions ($\mathbf{e}_u = \mathbf{U}/|\mathbf{U}|$).

In Figs. 3(d) and 4(d), we show the **k**-space distribution of **U** for the two bands. **U** of both bands swirls clockwise around $\bar{Y}$, indicating that the upper (lower) branch of them exhibits clockwise (counterclockwise) chiral texture around $\bar{Y}$ in agreement with the numerical results. Comparing the two figures, we observe that $|\mathbf{U}|$ for S_1 is considerably larger than that for S_2 in line with the α_R values in Table II. Above all, $|\mathbf{U}|$ for S_2 along $\bar{Y}\bar{\Gamma}$ is particularly small in accord with the surprisingly small α_R parameter, 0.02 eV Å for S_2 in Table II. Why **U** exhibits stronger anisotropy than **L** between $\bar{Y}\bar{\Gamma}$ and $\bar{Y}\bar{S}$ is explained as follows: Like **L**, **U** can be decomposed into $\mathbf{U} = \mathbf{U}^{(p)} + \mathbf{U}^{(d)}$ with the p and d components. If we ignore small dependence of $\langle\phi_{lm}|f_{\rm so}|\phi_{lm'}\rangle$'s on m and m' and approximate them by the atomic SOI parameter ξ_l, **U** can be expressed as $\mathbf{U} \approx \xi_p\mathbf{L}^{(p)} + \xi_d\mathbf{L}^{(d)}$. The point is that ξ_p is much larger than ξ_d for Au. Actually, according to Table I in Ref. [16], $\xi_p/\xi_d \sim 4.4$. Therefore, when $\mathbf{U}^{(p)}$ and $\mathbf{U}^{(d)}$ are summed up, the major component $\mathbf{U}^{(d)}$ is modified by $\mathbf{U}^{(p)}$ more significantly than $\mathbf{L}^{(d)}$ is modified by $\mathbf{L}^{(p)}$, leading to larger anisotropy between $\bar{Y}\bar{\Gamma}$ and $\bar{Y}\bar{S}$ of **U**. As a whole, the **k** distribution of **U** shown in Figs. 3(d) and 4(d) reproduces qualitatively very well the anisotropic spin-splitting energies of the two surface bands shown in Figs. 1(d) and 1(e).

B. Au(110)-(1 × 2) surface

Next, we present results for the missing-row reconstructed Au(110)-(1 × 2) surface, in which every second close-packed atomic row parallel to the $[\bar{1}10]$ (x) direction is removed from the topmost layer [41]. The short aspect of the SBZ in the [001] (y) direction is halved by the reconstruction as depicted in Fig. 1(b). The original $\bar{Y}$ and $\bar{S}$ points become equivalent to $\bar{\Gamma}$ and $\bar{X}$, and new zone boundary points, $\bar{Y}'$ with $\mathbf{k}_{\bar{Y}'} = (0, \frac{\pi}{2a})$ and $\bar{S}'$ with $\mathbf{k}_{\bar{S}'} = (\frac{\sqrt{2}\pi}{a}, \frac{\pi}{2a})$, are defined. We place the origin of the real-space coordinate again at one of the first-layer atoms. The surface structure is invariant with respect to four mirror reflection operators, i.e., $\hat{M}_x(0)$, $\hat{M}_x(\frac{a}{2\sqrt{2}})$, $\hat{M}_y(0)$, and $\hat{M}_y(a)$.

We show in Fig. 5(a) a logarithmic intensity plot of $\rho(\mathbf{k}, \varepsilon)$ for a first-layer surface atom. Due to the back-folding of bulk bands into the smaller SBZ, the surface-projected L-point bulk band gap is completely lost around $\bar{\Gamma}$ ($\bar{Y}$). Further, the S_2 band on the (1 × 1) surface, which is more strongly localized on the

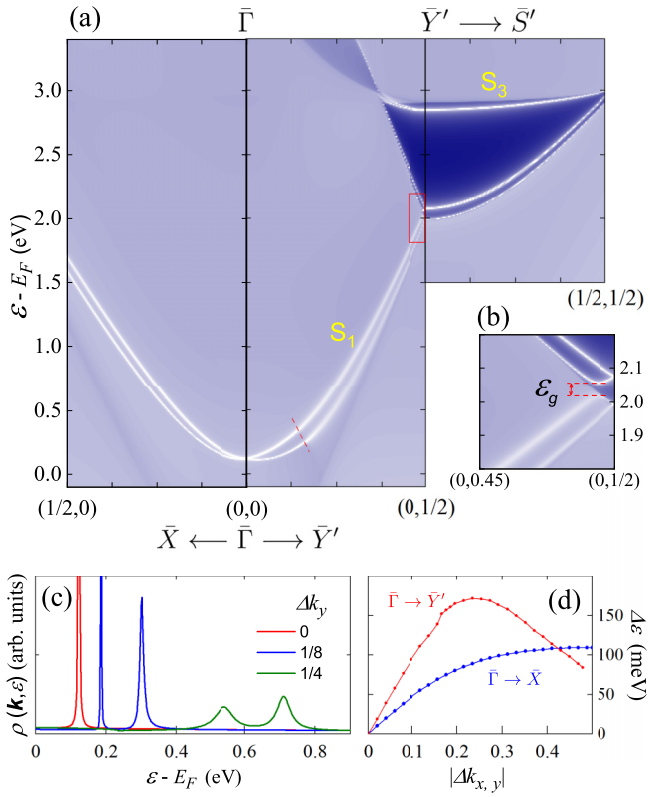

FIG. 5. (a) Logarithmic intensity plot of $\rho(\mathbf{k}, \varepsilon)$ for a first-layer atom on Au(110)-(1 × 2). Imaginary energy $\gamma = 0.5$ meV. (b) A magnified view of $\rho(\mathbf{k}, \varepsilon)$ for a first-layer atom within the boxed region marked by red solid line in panel (a). (c) $\rho(\mathbf{k}, \varepsilon)$ versus energy ε at $\mathbf{k} = (0, 0)$, $(0, \frac{1}{8})$, and $(0, \frac{1}{4})$ along $\bar{\Gamma}\bar{Y}'$. Imaginary energy $\gamma = 0$. (d) Spin-splitting energy of S_1 on Au(110)-(1 × 2) along $\bar{\Gamma}\bar{Y}'$ and $\bar{\Gamma}\bar{X}$ as a function of $\Delta\mathbf{k} = \mathbf{k} - \mathbf{k}_{\bar{\Gamma}}$ with $\mathbf{k}_{\bar{\Gamma}} = (0, 0)$. In all panels, wave vectors and wave numbers are given in units of $\frac{\pi}{a}$.

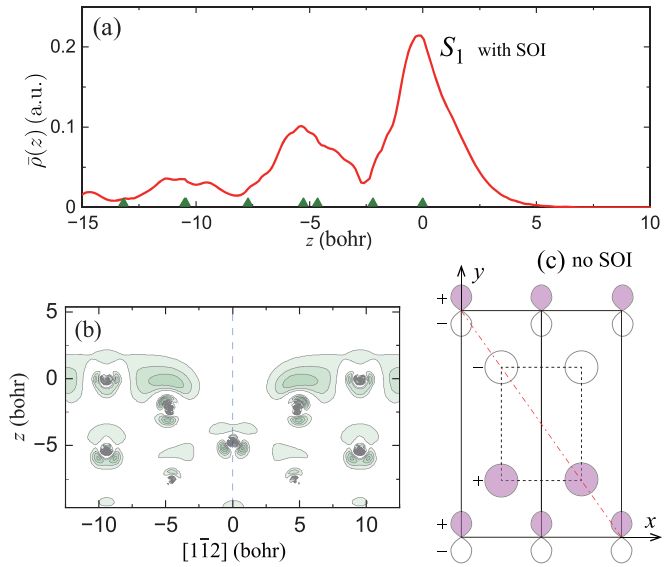

FIG. 6. (a) Planar-averaged charge density of the doubly degenerate S_1 at $\bar{\Gamma}$ ($\bar{Y}$) on Au(110)-(1 × 2) in the presence of SOI. Solid triangles on the z axis indicate z coordinates of Au atoms. Two triangles at around $z = -5$ a.u. arise due to a small buckling of atoms in the third layer. (b) Contour map of the same charge density as in panel (a) on a ($\bar{1}$11) vertical cut-plane indicated by dash-dotted line in panel (c). (c) Symmetry of the the wave function of S_1 at $\bar{\Gamma}$ in the absence of SOI. Solid rectangles are (1 × 2) unit cells of the topmost layer.

vacuum side of the topmost Au layer, disappears. On the other hand, the two spin-split branches of S_1 persist, although they become a surface resonance with a finite energy width due to hybridization with bulk states. Moreover, their energies shift upward by ∼0.7 eV as compared with those on the (1 × 1) surface. As a result, S_1 becomes an unoccupied band above E_F. The energy dispersion curves of S_1 near $\bar{\Gamma}$ in Fig. 5(a) are in good agreement with the ones in previous calculations [19,24,26]. The band minimum $E_0 = 0.12$ eV in the present calculation is a little lower than $E_0 = 0.35$ eV reported in a very recent inverse photoemission study [27]. A merit of the present semi-infinite surface calculation is that we can investigate not only the peak energy but also the energy width of a surface resonance. In Fig. 5(c), we plot $\rho(\mathbf{k}, \varepsilon)$ for a first-layer surface atom at three $\mathbf{k}$ points along $\bar{\Gamma}\bar{Y}'$ with $k_y = 0$, $\frac{\pi}{8a}$, and $\frac{\pi}{4a}$. The two DOS peaks at $k_y = \frac{\pi}{4a}$ are seen to be much broader than those at the other points. This occurs since the dispersion curves of $S_1^{(+)}$ and $S_1^{(-)}$ cross the boundary of a surface-projected bulk band marked by red dashed line in Fig. 5(a) and merged into the energy region of one more surface-projected bulk bands between $k_y = \frac{\pi}{8a}$ and $\frac{\pi}{4a}$.

Remarkably, $S_1^{(+)}$ and $S_1^{(-)}$ persist up to the zone boundary $\bar{Y}'$ despite orbital hybridization with bulk states and become localized surface states in a narrow $\mathbf{k}$-space region near $\bar{Y}'\bar{S}'$, where the surface-projected bulk band gap survives the back-folding of bulk bands. Figure 5(b) shows a magnified view of $\rho(\mathbf{k}, \varepsilon)$ within the boxed region marked by red solid line in panel (a). It is seen that the dispersion curves of $S_1^{(+)}$ and $S_1^{(-)}$ exhibit a mini band gap ε_g associated with the (1 × 2) superlattice potential near the zone boundary $\bar{Y}'$. Similar mini gaps were recently observed for the L-gap surface state on the Au(111)-(22 × $\sqrt{3}$) surface [39].

In Fig. 5(d), we show the spin-splitting energies of S_1 along two symmetry lines as a function of $\Delta\mathbf{k} = \mathbf{k} - \mathbf{k}_{\bar{\Gamma}} = \mathbf{k}$. The $\Delta\varepsilon$ curve for $\bar{\Gamma}\bar{Y}'$ exhibits a nonsmooth behavior at $k_y \sim 0.15\frac{\pi}{a}$, at which the dispersion curves of S_1 cross the boundary of a surface-projected bulk band as mentioned above. We fitted the energy dispersion with $\mathbf{k}$ of the two spin-split branches by using Eq. (2). The effective masses and the Rashba parameters are listed in Table II. By comparing the (1 × 1) and (1 × 2) surfaces, we see that m^* of S_1 is significantly modified by the reconstruction.

Here, we address briefly the real-space behavior of the wave function of S_1. In Fig. 6(a), we show the planar averaged charge density of the doubly degenerate S_1 at $\bar{\Gamma}$ on Au(110)-(1 × 2), which resembles that of S_1 on the (1 × 1) surface in Fig. 2(a). In Fig. 6(b), we plot the contour map of the same charge density as in Fig. 6(a) on a ($\bar{1}$11) vertical cut plane shown by a red dash-dotted line in Fig. 6(c), which agrees well with the one in the work of Nagano *et al.* [26]. In Fig. 6(c), we illustrate the real-space symmetry of S_1 at $\bar{\Gamma}$ in the absence of SOI. The spatial part of its wave function is odd with respect to $\hat{M}_y(0)$ and $\hat{M}_y(a)$, and even with respect

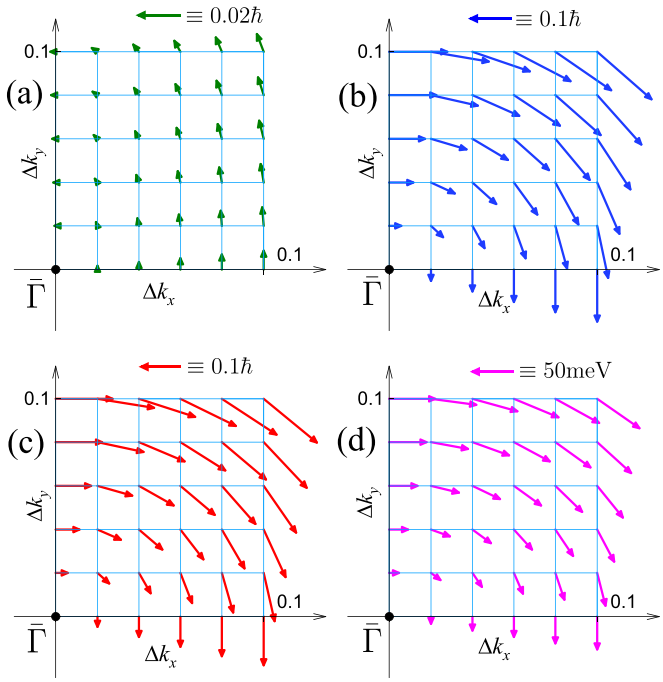

FIG. 7. The **k**-space distribution around $\bar{\Gamma}$ of (a) $\mathbf{L}^{(p)}$, (b) $\mathbf{L}^{(d)}$, and (c) the total OAM $\mathbf{L}$ for the S_1 band on Au(110)-(1 × 2) in the absence of SOI. (d) Vector field $\mathbf{U}$ inducing the spin splitting of the S_1 band around $\bar{\Gamma}$. In all panels, Δk_x and Δk_y are given in units of $\frac{\pi}{a}$.

to $\hat{M}_x(0)$ and $\hat{M}_x(\frac{a}{2\sqrt{2}})$. As mentioned before, when SOI is present, the orbital components with opposite spin directions and opposite spatial parities are slightly mixed.

We now show that the anisotropic spin splitting of the S_1 band is driven by the OAM, following the same procedure as that in the preceding section. To do so, we first need to calculate $\mathbf{L}$ and $\mathbf{U}$ of S_1 in the absence of SOI. This is not an obvious task in the present case because S_1 is a resonance hybridized with bulk states. Fortunately, as seen from Fig. 5(b), the DOS peaks of S_1 are very sharp near $\bar{\Gamma}$ (say $|\mathbf{k}| < 0.1\frac{\pi}{a}$) and much larger than the nearly constant background DOS of bulk states. Thus, we calculated the two quantities approximately by evaluating the contributions to $\mathbf{L}$ and $\mathbf{U}$ of all one-electron states with energy ε from the Green's function and further integrating these quantities over an energy interval containing the full DOS peak of S_1. We show in Fig. 7 the **k**-space distributions of $\mathbf{L}^{(p)}$, $\mathbf{L}^{(d)}$, $\mathbf{L}$, and $\mathbf{U}$ calculated in this way. They are seen to behave similarly to the corresponding ones on the (1 × 1) surface shown in Fig. 3. The major component $\mathbf{L}^{(d)}$ exhibits a clockwise chiral texture around $\bar{\Gamma}$ and weak anisotropy between $\bar{\Gamma}\bar{Y}'$ and $\bar{\Gamma}\bar{X}$. Since $|\mathbf{L}^{(d)}|$ is much larger than $|\mathbf{L}^{(p)}|$, the total OAM in panel (c) looks similar to $\mathbf{L}^{(d)}$ in panel (b). The vector field $\mathbf{U}$ in panel (d) exhibits also a clockwise chiral texture. Comparing $\mathbf{L}$ and $\mathbf{U}$, we see that the anisotropy between $\bar{\Gamma}\bar{Y}'$ and $\bar{\Gamma}\bar{X}$ in the **k**-space distribution of $\mathbf{U}$ is larger than that of $\mathbf{L}$ by the same reason as discussed for the (1 × 1) surface. From the overall agreement between $2|\mathbf{U}|$ in Fig. 7(d) and $\Delta\varepsilon$ in Fig. 5(d), we conclude that the spin splitting of S_1 is driven by the OAM and its anisotropy is enhanced by the difference in atomic SOI parameters between the p and d orbitals.

C. OAM in the presence of SOI

So far, we have studied the OAM of surface bands in the absence of SOI. While this is appropriate from the viewpoint of calculating $\Delta\varepsilon$ by perturbation theory, it may be of interest to examine how the OAM calculated without SOI is modified when SOI is turned on.

Let $\{\Phi_0, \Phi_1, \Phi_2, \cdots\} \otimes \{|+1\rangle, |-1\rangle\}$ be the complete set of the eigenfunctions of the Hamiltonian with $\mathbf{k}$ in the absence of SOI, where Φ_n is the spatial part of the wave function, and $|+1\rangle$ and $|-1\rangle$ are spin wave functions for the up-spin and down-spin states. We denote the total wave function of an electron by $\Psi_{n,\alpha} \equiv \Phi_n|\alpha\rangle$ ($\alpha = \pm 1$) and its energy in the absence of SOI by ε_n. Now, let Φ_0 be the surface state of our interest. We calculate $\mathbf{U}$ defined by Eq. (6) for Φ_0 and choose $\mathbf{e}_u$ as the spin quantization axis so $\hat{H}_{\rm so}$ becomes diagonal with respect to $\{\Psi_{0,+1}, \Psi_{0,-1}\}$. Then, the change in $\Psi_{0,\alpha}$ in the presence of SOI is given to the first order of $\hat{H}_{\rm so}$ by

$$\Delta\Psi_{0,\alpha} = \sum_{n\neq 0}\sum_{\beta=\pm 1} \Psi_{n,\beta}\frac{\langle\Psi_{n,\beta}|\hat{H}_{\rm so}|\Psi_{0,\alpha}\rangle}{\varepsilon_0 - \varepsilon_n}, \tag{7}$$

which means that the change in $\mathbf{L}$ of $\Psi_{0,\alpha}$ is given by

$$\Delta\mathbf{L}_{(\alpha)} = 2\mathrm{Re}\sum_{n\neq 0}\sum_{\beta=\pm 1}\frac{\langle\Psi_{0,\alpha}|\vec{L}|\Psi_{n,\beta}\rangle\langle\Psi_{n,\beta}|\hat{H}_{\rm so}|\Psi_{0,\alpha}\rangle}{\varepsilon_0 - \varepsilon_n}. \tag{8}$$

Since $\vec{L}$ is spin-diagonal, β in Eq. (8) must be equal to α. Then, the second matrix element is simplified as

$$\langle\Psi_{n,\alpha}|\hat{H}_{\rm so}|\Psi_{0,\alpha}\rangle = \alpha\langle\Phi_n|\sum_a f_a(r)(\vec{L}_a)_u|\Phi_0\rangle, \tag{9}$$

where we used the fact that the matrix elements of the Pauli matrices are given by $\langle\alpha|\sigma_u|\alpha\rangle = \alpha$ and $\langle\alpha|\sigma_{v,w}|\alpha\rangle = 0$, where the u axis is parallel to $\mathbf{e}_u$, and the v and w axes are orthogonal to $\mathbf{e}_u$. From Eqs. (8) and (9), we obtain $\Delta\mathbf{L}_{(\pm)} = \pm\Delta\mathbf{L}$ with $\Delta\mathbf{L}$ defined by

$$\Delta\mathbf{L} = 2\mathrm{Re}\sum_{n\neq 0}\frac{\langle\Phi_0|\vec{L}|\Phi_n\rangle\langle\Phi_n|\sum_a f_a(r)(\vec{L}_a)_u|\Phi_0\rangle}{\varepsilon_0 - \varepsilon_n}, \tag{10}$$

which indicates that when SOI is turned on, $\mathbf{L}$'s of the upper and lower spin-split bands change in the opposite directions by the same amount.

As an example, we show in Fig. 8 $(\mathbf{L})_y$ versus Δk_x of the S_1 band on Au(110)-(1 × 1) along $\bar{Y}\bar{S}$, on which $(\mathbf{L})_{x,z}$ vanishes due to mirror reflection symmetry $\hat{M}_y(0)$. We denote $\mathbf{L}$ of $S_1^{(+)}$, $\mathbf{L}$ of $S_1^{(-)}$, and $\mathbf{L}$ in the absence of SOI by $\mathbf{L}_{(+)}$, $\mathbf{L}_{(-)}$, and $\mathbf{L}_0$, respectively. In Figs. 8(a) and 8(b), we plot the p and d components of these three quantities by red, blue, and green lines. The dashed magenta lines in both panels show the p and d components of the average of $\mathbf{L}_{(+)}$ and $\mathbf{L}_{(-)}$. As seen, for both the p and d components, $\mathbf{L}_{(+)}$ and $\mathbf{L}_{(-)}$ split in opposite directions from $\mathbf{L}_0$. That the average of $\mathbf{L}_{(+)}$ and $\mathbf{L}_{(-)}$ (dashed lines) agrees well with $\mathbf{L}_0$ (green lines) signifies that Eq. (10) derived by perturbation theory holds well. The difference between the two lines may be attributed to the higher-order terms not included in Eq. (10).

Since $|(\mathbf{L}_0^{(p)})_y|$ (green line) is smaller than $|(\Delta\mathbf{L}^{(p)})_y|$, $(\mathbf{L}_{(+)}^{(p)})_y$ and $(\mathbf{L}_{(-)}^{(p)})_y$ in Fig. 8(a) possess positive and negative signs. This means that the p component of $\mathbf{L}_{(+)}$ and $\mathbf{L}_{(-)}$

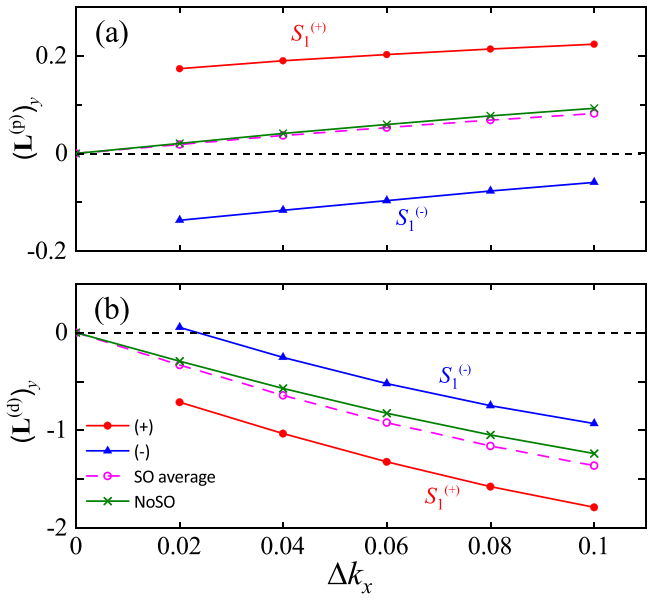

FIG. 8. (a) $(\mathbf{L}^{(p)})_y$ and (b) $(\mathbf{L}^{(d)})_y$ of the S_1 band on Au(110)-(1×1) along $\bar{Y}\bar{S}$ as a function of $\Delta\mathbf{k} = \mathbf{k} - \mathbf{k}_{\bar{Y}}$ with $\mathbf{k}_{\bar{Y}} = (0, \frac{\pi}{a})$. In both panels, red, blue, and green lines correspond to $\mathbf{L}_{(+)}$, $\mathbf{L}_{(-)}$, and $\mathbf{L}_0$, respectively. The dashed magenta lines in both panels show the average of $\mathbf{L}_{(+)}$ and $\mathbf{L}_{(-)}$. $\mathbf{L}$ is given in units of $0.1\hbar$ and Δk_x in units of $\frac{\pi}{a}$.

exhibits counterclockwise and clockwise chiral textures in the $\mathbf{k}$ space, respectively. This feature was also observed for the L-gap surface state on Au(111) in the paper of Kim *et al.* [3]. On the other hand, since $|(\mathbf{L}_0^{(d)})_y|$ is larger than $|(\Delta\mathbf{L}^{(d)})_y|$ $(\Delta k_x > 0.02\frac{\pi}{a})$, both $(\mathbf{L}_{(+)}^{(d)})_y$ and $(\mathbf{L}_{(-)}^{(d)})_y$ in Fig. 8(b) possess negative signs. This means that the d component of both $\mathbf{L}_{(+)}$ and $\mathbf{L}_{(-)}$ exhibits a clockwise chiral texture in the $\mathbf{k}$ space. This was also the case for the L-gap surface state on Au(111) [3].

IV. SUMMARY

We studied the L-gap surface states on semi-infinite clean Au(110) surfaces by first-principles DFT calculations. On the (1×1) surface, two surface bands, the partially occupied S_1 and the unoccupied S_2, appear within the surface-projected L-point bulk band gap. We calculated the energy dispersion with $\mathbf{k}$ of both bands and discussed the symmetry of their wave functions. On the missing-row reconstructed (1×2) surface, the projected bulk band gap is mostly lost due to the back-folding of bulk bands. As a result, S_2 disappears while S_1 persists as an unoccupied surface resonance. We calculated not only the spin-split peak energies but also the energy widths of S_1 as a function of $\mathbf{k}$.

For both surfaces, we discussed the physical mechanism of strongly anisotropic spin-splitting energies of the surface bands in terms of the orbital Rashba effect. For this purpose, we first calculated $\mathbf{L}$, the OAM of the surface bands in the absence of SOI. Then, by applying perturbation theory, we derived a vector field $\mathbf{U}$, which can be approximated as $\mathbf{U} \approx \xi_p\mathbf{L}^{(p)} + \xi_d\mathbf{L}^{(d)}$, where $\mathbf{L}^{(p)}$ and $\mathbf{L}^{(d)}$ are the p and d components of $\mathbf{L}$ of the surface band under consideration, and ξ_p and ξ_d are the atomic SOI parameters for the Au p and d orbitals. The spin-splitting energy of the surface band, $\Delta\varepsilon$, is given by $\Delta\varepsilon = 2|\mathbf{U}|$, and its upper and lower branches are spin-polarized parallel and antiparallel to $\mathbf{U}$. It was found that the major component $\mathbf{L}^{(d)}$ for S_1 and S_2 is only weakly anisotropic in the $\mathbf{k}$-space, whereas the minor component $\mathbf{L}^{(p)}$ is more anisotropic and oriented opposite $\mathbf{L}^{(d)}$. Most importantly, since ξ_p is several times larger than ξ_d, the resultant $\mathbf{U}$ becomes more anisotropic than $\mathbf{L}$ and is able to explain the anisotropic $\Delta\varepsilon$ and the chiral spin textures of S_1 and S_2 well. Specifically, with this scenario, we can explain why the Rashba parameter for S_2 along $\bar{Y}\bar{\Gamma}$ on Au(110)-(1×1) becomes exceptionally small. We have also clarified how $\mathbf{L}$ of a surface band calculated without SOI is modified in the presence of SOI. Our analysis suggests that the expression $\mathbf{U} \approx \xi_p\mathbf{L}^{(p)} + \xi_d\mathbf{L}^{(d)}$ may hold if $\mathbf{L}$ in this expression is replaced by the OAM averaged over the two spin-split surface bands.

ACKNOWLEDGMENTS

This work is supported by the Japan Society for the Promotion of Science KAKENHI, Grants No. JP20K05333 and No. JP22H01960.

[1] S. R. Park, C. H. Kim, J. Yu, J. H. Han, and C. Kim, Orbital-Angular-Momentum Based Origin of Rashba-Type Surface Band Splitting, Phys. Rev. Lett. **107**, 156803 (2011).

[2] J.-H. Park, C. H. Kim, J.-W. Rhim, and J. H. Han, Orbital Rashba effect and its detection by circular dichroism angle-resolved photoemission spectroscopy, Phys. Rev. B **85**, 195401(R) (2012).

[3] B. Kim, C. H. Kim, P. Kim, W. Jung, Y. Kim, Y. Koh, M. Arita, K. Shimada, H. Namatame, M. Taniguchi, J. Yu, and C. Kim, Spin and orbital angular momentum structure of Cu(111) and Au(111) surface states, Phys. Rev. B **85**, 195402 (2012).

[4] P. Kim, K. T. Kang, G. Go, and J. H. Han, Nature of orbital and spin Rashba coupling in the surface bands of $SrTiO_3$ and $KTaO_3$, Phys. Rev. B **90**, 205423 (2014).

[5] S. R. Park, J. Han, C. Kim, Y. Y. Koh, C. Kim, H. Lee, H. J. Choi, J. H. Han, K. D. Lee, N. J. Hur, M. Arita, K. Shimada, H. Namatame, and M. Taniguchi, Chiral Orbital-Angular Momentum in the Surface States of Bi_2Se_3, Phys. Rev. Lett. **108**, 046805 (2012).

[6] D. Go, J.-P. Hanke, P. M. Buhl, F. Freimuth, G. Bihlmayer, H.-W. Lee, Y. Mokrousov, and S. Blügel, Toward surface orbitronics: Giant orbital magnetism from the orbital Rashba effect at the surface of *sp*-metals, Sci. Rep. **7**, 46742 (2017).

[7] S. Oh and H. J. Choi, Orbital angular momentum analysis for giant spin splitting in solids and nanostructures, Sci. Rep. **7**, 2024 (2017).

[8] M. Ünzelmann, H. Bentmann, P. Eck, T. Kißlinger, B. Geldiyev, J. Rieger, S. Moser, R. C. Vidal, K. Kißner, L. Hammer, M. A.

Schneider, T. Fauster, G. Sangiovanni, D. Di Sante, and F. Reinert, Orbital-Driven Rashba Effect in a Binary Honeycomb Monolayer AgTe, Phys. Rev. Lett. **124**, 176401 (2020).

[9] T. Kobayashi, Y. Nakata, K. Yaji, T. Shishidou, D. Agterberg, S. Yoshizawa, F. Komori, S. Shin, M. Weinert, T. Uchihashi, and K. Sakamoto, Orbital Angular Momentum Induced Spin Polarization of 2D Metallic Bands, Phys. Rev. Lett. **125**, 176401 (2020).

[10] D. Go, D. Jo, T. Gao, K. Ando, S. Blügel, H.-W. Lee, and Y. Mokrousov, Orbital Rashba effect in a surface-oxidized cu film, Phys. Rev. B **103**, L121113 (2021).

[11] Y. A. Bychkov and E. I. Rashba, Properties of a 2D electron gas with lifted spectral degeneracy, JETP Lett. **39**, 78 (1984).

[12] S. LaShell, B. A. McDougall, and E. Jensen, Spin Splitting of an Au(111) Surface State Band Observed with Angle Resolved Photoelectron Spectroscopy, Phys. Rev. Lett. **77**, 3419 (1996).

[13] G. Nicolay, F. Reinert, S. Hüfner, and P. Blaha, Spin-orbit splitting of the L-gap surface state on Au(111) and Ag(111), Phys. Rev. B **65**, 033407 (2001).

[14] A. Tamai, W. Meevasana, P. D. C. King, C. W. Nicholson, A. de la Torre, E. Rozbicki, and F. Baumberger, Spin-orbit splitting of the Shockley surface state on Cu(111), Phys. Rev. B **87**, 075113 (2013).

[15] H. Lee and H. J. Choi, Role of d orbitals in the Rashba-type spin splitting for noble-metal surfaces, Phys. Rev. B **86**, 045437 (2012).

[16] H. Ishida, Rashba spin splitting of Shockley surface states on semi-infinite crystals, Phys. Rev. B **90**, 235422 (2014).

[17] A. Goldmann, V. Dose, and G. Borstel, Empty electronic states at the (100), (110), and (111) surfaces of nickel, copper, and silver, Phys. Rev. B **32**, 1971 (1985).

[18] R. A. Bartynski and T. Gustafsson, Experimental study of surface states on the (110) faces of the noble metals, Phys. Rev. B **33**, 6588 (1986).

[19] C. H. Xu, K. M. Ho, and K. P. Bohnen, Self-consistent calculation of the surface electronic structure of the (1×2) reconstructed Au(110) surface, Phys. Rev. B **39**, 5599 (1989).

[20] R. Drube, V. Dose, H. Derks, and W. Heiland, The 1×1 to 1×2 phase-transition on Au(110): An inverse photoemission-study, Surf. Sci. **214**, L253 (1989).

[21] A. Gerlach, G. Meister, R. Matzdorf, and A. Goldmann, High-resolution photoemission study of the $\bar{Y}$ surface state on Ag(110), Surf. Sci. **443**, 221 (1999).

[22] P. Straube, F. Pforte, T. Michalke, K. Berge, A. Gerlach, and A. Goldmann, Photoemission study of the surface state at $\bar{Y}$ on Cu(110): Band structure, electron dynamics, and surface optical properties, Phys. Rev. B **61**, 14072 (2000).

[23] O. Zeybek, A. M. Davarpanah, and S. D. Barrett, Electronic surface states of Cu(110) surface, Surf. Sci. **600**, 5176 (2006).

[24] A. Nuber, M. Higashiguchi, F. Forster, P. Blaha, K. Shimada, and F. Reinert, Influence of reconstruction on the surface state of Au(110), Phys. Rev. B **78**, 195412 (2008).

[25] J. Jiang, S. S. Tsirkin, K. Shimada, H. Iwasawa, M. Arita, H. Anzai, H. Namatame, M. Taniguchi, I. Y. Sklyadneva, R. Heid, K. P. Bohnen, P. M. Echenique, and E. V. Chulkov, Many-body interactions and Rashba splitting of the surface state on Cu(110), Phys. Rev. B **89**, 085404 (2014).

[26] M. Nagano, A. Kodama, T. Shishidou, and T. Oguchi, A first-principles study on the Rashba effect in surface systems, J. Phys.: Condens. Matter **21**, 064239 (2009).

[27] K. T. Ritter, K. Miyamoto, T. Okuda, and M. Donath, Rashba-type splitting of the Au(110) surface state: A combined inverse and direct photoemission study, Phys. Rev. B **104**, L161101 (2021).

[28] J. P. Perdew, K. Burke, and M. Ernzerhof, Generalized Gradient Approximation Made Simple, Phys. Rev. Lett. **77**, 3865 (1996).

[29] G. Kresse and J. Hafner, *Ab initio* molecular dynamics for liquid metals, Phys. Rev. B **47**, 558 (1993).

[30] G. Kresse and J. Furthmüller, Efficiency of *ab-initio* total energy calculations for metals and semiconductors using a plane-wave basis set, Comput. Mater. Sci. **6**, 15 (1996).

[31] P. E. Blöchl, Projector augmented-wave method, Phys. Rev. B **50**, 17953 (1994).

[32] J. Inglesfield, A method of embedding, J. Phys. C **14**, 3795 (1981).

[33] J. Inglesfield, *The Embedding Method for Electronic Structure* (IOP Publishing, Bristol, 2015).

[34] D. J. Singh and L. Nordstrom, *Planewaves, Pseudopotentials, and the LAPW Method*, 2nd ed. (Springer, New York, 2006).

[35] M. James and S. Crampin, Relativistic embedding method: The transfer matrix, complex band structures, transport, and surface calculations, Phys. Rev. B **81**, 155439 (2010).

[36] A. Nuber, J. Braun, F. Forster, J. Minar, F. Reinert, and H. Ebert, Surface versus bulk contributions to the Rashba splitting in surface systems, Phys. Rev. B **83**, 165401 (2011).

[37] A. Bendounan, K. Ait-Mansour, J. Braun, J. Minar, S. Bornemann, R. Fasel, O. Groning, F. Sirotti, and H. Ebert, Evolution of the Rashba spin-orbit-split Shockley state on Ag/Pt(111), Phys. Rev. B **83**, 195427 (2011).

[38] A. L. Kutepov, Elimination of the linearization error in APW/LAPW basis set: Dirac-Kohn-Sham equations, Phys. Rev. B **103**, 165101 (2021).

[39] H. Ishida, Spin-dependent band-gap formation for the L-gap surface state on the reconstructed Au(111) surface, J. Phys.: Condens. Matter **34**, 195002 (2022).

[40] E. Simon, A. Szilva, B. Ujfalussy, B. Lazarovits, G. Zarand, and L. Szunyogh, Anisotropic Rashba splitting of surface states from the admixture of bulk states: Relativistic *ab initio* calculations and $\boldsymbol{k} \cdot \boldsymbol{p}$ perturbation theory, Phys. Rev. B **81**, 235438 (2010).

[41] D. D. dos Reis, F. R. Negreiros, V. E. de Carvalho, and E. A. Soares, Geometry of the Au(110)-(1×2) missing-row clean surface: A New LEED and DFT study, Surf. Sci. **604**, 568 (2010).